07 Oct 2023

Ab Initio Quantum Scattering Calculations and a New Potential Energy Surface for the HCl($X^1\Sigma$+)-O2(X 3 Σ G −) System: Collision-Induced Line Shape Parameters for O2-Perturbed R(0) 0-0 Line in H35Cl

Artur Olejnik

Hubert Jóźwiak

Maciej Gancewski

Ernesto Quintas-Sánchez
Missouri University of Science and Technology, quintassancheze@mst.edu

et. al. For a complete list of authors, see https://scholarsmine.mst.edu/chem_facwork/3650

Recommended Citation

A. Olejnik et al., "Ab Initio Quantum Scattering Calculations and a New Potential Energy Surface for the HCl($X^1\Sigma$+)-O2(X 3 Σ G −) System: Collision-Induced Line Shape Parameters for O2-Perturbed R(0) 0-0 Line in H35Cl," *Journal of Chemical Physics*, vol. 159, no. 13, article no. 134301, American Institute of Physics, Oct 2023.
The definitive version is available at https://doi.org/10.1063/5.0169968

The Journal of Chemical Physics

RESEARCH ARTICLE | OCTOBER 02 2023

Ab initio quantum scattering calculations and a new potential energy surface for the HCl($X^1\Sigma^+$)–O_2($X^3\Sigma_g^-$) system: Collision-induced line shape parameters for O_2-perturbed R(0) 0–0 line in $H^{35}Cl$

Artur Olejnik ✉ ; Hubert Jóźwiak ; Maciej Gancewski ; Ernesto Quintas-Sánchez ; Richard Dawes ;
Piotr Wcisło

Check for updates

J. Chem. Phys. 159, 134301 (2023)
https://doi.org/10.1063/5.0169968

View Online Export Citation CrossMark

Articles You May Be Interested In

Nuclear Magnetic Hyperfine Spectra of $H^{35}Cl$ and $H^{37}Cl$

J. Chem. Phys. (September 2003)

Temperature dependence of resonant isotopic vibrational energy transfer in $H^{35}Cl$–H^{37} Cl

J. Chem. Phys. (July 2008)

Investigation of the ground vibrational state structure of $H^{35}Cl$ trimer based on the resolved *K*, *J* substructure of the v $_5$ vibrational band

J. Chem. Phys. (May 1994)

AIP Publishing

Ab initio quantum scattering calculations and a new potential energy surface for the HCl($X^1\Sigma^+$)–O_2($X^3\Sigma_g^-$) system: Collision-induced line shape parameters for O_2-perturbed R(0) 0–0 line in $H^{35}Cl$

Cite as: J. Chem. Phys. 159, 134301 (2023); doi: 10.1063/5.0169968
Submitted: 30 July 2023 • Accepted: 1 September 2023 •
Published Online: 2 October 2023

Artur Olejnik,[1,a)] **Hubert Jóźwiak,**[1] **Maciej Gancewski,**[1] **Ernesto Quintas-Sánchez,**[2]
Richard Dawes,[2] **and Piotr Wcisło**[1,b)]

AFFILIATIONS

[1] Institute of Physics, Faculty of Physics, Astronomy and Informatics, Nicolaus Copernicus University in Toruń, Grudziądzka 5, 87-100 Toruń, Poland

[2] Department of Chemistry, Missouri University of Science and Technology, Rolla, Missouri 65409-0010, USA

[a)] **Author to whom correspondence should be addressed:** artur.olejnik.umk@gmail.com
[b)] **E-mail:** piotr.wcislo@umk.pl

ABSTRACT

The remote sensing of abundance and properties of HCl—the main atmospheric reservoir of Cl atoms that directly participate in ozone depletion—is important for monitoring the partitioning of chlorine between "ozone-depleting" and "reservoir" species. Such remote studies require knowledge of the shapes of molecular resonances of HCl, which are perturbed by collisions with the molecules of the surrounding air. In this work, we report the first fully quantum calculations of collisional perturbations of the shape of a pure rotational line in $H^{35}Cl$ perturbed by an air-relevant molecule [as the first model system we choose the R(0) line in HCl perturbed by O_2]. The calculations are performed on our new highly accurate $HCl(X^1\Sigma^+)–O_2(X^3\Sigma_g^-)$ potential energy surface. In addition to pressure broadening and shift, we also determine their speed dependencies and the complex Dicke parameter. This gives important input to the community discussion on the physical meaning of the complex Dicke parameter and its relevance for atmospheric spectra (previously, the complex Dicke parameter for such systems was mainly determined from phenomenological fits to experimental spectra and the physical meaning of its value in that context is questionable). We also calculate the temperature dependence of the line shape parameters and obtain agreement with the available experimental data. We estimate the total combined uncertainties of our calculations at 2% relative root-mean-square error in the simulated line shape at 296 K. This result constitutes an important step toward computational population of spectroscopic databases with accurate *ab initio* line shape parameters for molecular systems of terrestrial atmospheric importance.

I. INTRODUCTION

The ozone layer protecting the Earth from harmful ultraviolet radiation is destroyed in chemical reactions induced in the stratosphere mainly by chlorofluorocarbons (CFCs), whose heightened atmospheric presence is of anthropogenic origin.[1,2] The discovery of the Antarctic ozone hole[3] stimulated and accelerated the ratification, in 1987, of the Montreal Protocol—an international agreement to reduce the production and emission of various ozone-depleting substances. As a direct impact of this treaty, now signed by all the United Nations members,[4] the concentration of the ozone-depleting compounds in our planet's atmosphere has been reduced[5,6] and the ozone layer over the Antarctica has started to recover,[7] which elevated the role of the Montreal Protocol as one of the most successful ongoing global human ecosystem initiatives.[8]

Among the ozone-depleting species originating from the breakdown of CFCs, atomic fluorine F and chlorine Cl are the most abundant.[2] These halogens react with other molecular constituents of Earth's atmosphere, forming acids and nitrates that result in the formation of stratospheric reservoirs of F and Cl. In the case of fluorine, the abstraction of hydrogen allows HF molecules to be formed, which due to their resilience to further photo-chemical breakdown keep the total amount of ozone-depleting FO molecules at negligible levels.[2] Thus, although fluorine itself has a relatively low impact on the ozone layer, the concentration of stratospheric HF may reflect the rate and distribution of the emission of surface-released fluorine-bearing gases.[1] On the other hand, the main stratospheric reservoirs of chlorine are HCl and $ClONO_2$, which are broken-up by photolysis and temperature-induced processes, thus feeding the ClO_x catalytic cycle: ozone depletion by Cl ($Cl + O_3 \rightarrow ClO + O_2$) and the subsequent provision of chlorine atoms ($ClO + O \rightarrow Cl + O_2$).[1,2,9] As most of the stratospheric chlorine resides in the hydrochloric acid reservoir,[2] the monitoring of HCl abundance using spectroscopic and remote-sensing techniques is necessary for the determination of the chlorine-partitioning between the "reservoir" HCl and "active" Cl and ClO that directly participate in ozone-depleting processes.[1,2,9]

Beyond the Earth's atmosphere, HCl spectra have been observed in various astrophysical conditions. Traces of hydrochloric acid were detected in the Venusian[10] and stellar[11] atmospheres. HCl absorption lines were also detected in one of the largest molecular gas clouds in our Galaxy, *Sagittarius* B2, against its dust continuum.[12] This observation pointed to the validity of the prediction of Jura[13] and Dalgarno *et al.*[14] that chlorine reservoirs in the cosmic molecular gas clouds should be deposited mostly in HCl and that for very dense clouds the cooling due to HCl can be surprisingly effective, comparable in its effect to CO molecules. Due to relatively low pressures typical for the interstellar medium, the shape of the HCl emission spectra can be well described without considerations involving collisional processes. However, as far as terrestrial-atmospheric applications are concerned, the shapes and positions of the lines in the required spectra are perturbed by collisions with other molecules, whose presence cannot be neglected. Various molecular transitions in such foreign gas-perturbed HCl that contribute to its atmospheric absorption spectrum have been studied extensively in the past, mostly in experiment[15–27] and less in theoretical works.[28–30]

HCl is a simple system of great interest in the spectroscopy of small molecules owing, in part, to its large rotational constant and permanent dipole moment. The spectral lines of HCl are, therefore, intense and relatively well separated, which allows for accurate probing of the beyond-Voigt line shape effects, in particular the Dicke narrowing,[31] especially pronounced in the rotation-vibration spectra of HCl.[32,33] The temperature- and pressure-dependent line shape perturbations examined in experimental and theoretical works mentioned above were studied for HCl interacting with N_2[18–21,23–26] and O_2[18,20,21,23–25]—the two most abundant constituents of the Earth's atmosphere—as well as with the noble gases: He,[26,28,34] Ar,[19,25,26,28–30,33,34] Kr,[34] and Xe,[26,28,34] with CF_4,[34] and with the hydrogen isotopologues: H_2 and D_2.[18] The self-perturbation effects on the line shape in the pure HCl mixtures were also studied.[32,35,36]

As far as the laboratory studies are concerned, a well-known problem with handling HCl is its highly corrosive and adsorptive nature.[19,23,25,27,29] Due to sticking of the individual molecules on the inner walls of the gas cell, the collision-induced line shape parameters determined from independent measurements may differ depending on the experimental approach and the measurement conditions (involving, e.g., the type of absorption cell surface, flowing, or static measurement approach).[23] Theoretical calculations of the collision-induced line shape parameters of HCl, performed *ab initio*, can thus provide valuable guidance in the interpretation and possible refinement of the measurements' results.

Previous theoretical studies of the line shape parameters of the HCl lines, which go beyond fitting experimental spectra with phenomenological line shape profiles, concern only the case of atom-perturbed HCl lines. For example, in an paper by Fitz and Marcus,[28] the half-widths and shifts of the HCl lines due to collisions with Ar and He are calculated using a semi-classical approach developed by Marcus[37] and Miller[38] (see Ref. 39 and references therein). In recent papers, Tran and Domenech[29] and Tran *et al.*[30] simulated the Ar-perturbed spectra of HCl directly using classical molecular dynamics simulations, utilizing a requantization procedure for determining the angular momentum quantum numbers corresponding to classical (continuous) angular frequencies. The relevant line shape parameters, such as the Lorentzian half-width and the Dicke parameter, were subsequently extracted from the simulated spectrum by fitting it with a beyond-Voigt line shape model.

It turns out, however, that no systematic efforts have been undertaken to determine the line shape parameters for the HCl spectra perturbed by collisions with diatomic molecules starting directly from the first principles of quantum mechanics. In this work, we report the first fully quantum calculations of collisional perturbations of the shape of a pure rotational line in HCl perturbed by an air-relevant molecule [as the first model system we choose the R(0) line in HCl perturbed by O_2].

We report a new *ab initio* potential energy surface (PES) for the $HCl(X^1\Sigma^+)–O_2(X^3\Sigma_g^-)$ system, and we use it to determine the S-matrices required for the computation of the generalized spectroscopic cross sections by solving numerically the relevant close-coupling equations employing the scattering boundary conditions. By averaging the cross sections over the collisional kinetic energies, we obtain the collisional line shape parameters: the pressure broadening and shift, the speed-dependence of broadening and shift, and the real and imaginary parts of the Dicke-narrowing parameter. The parameters are determined for temperatures ranging from 150 to 360 K. This work constitutes an important step toward populating line-by-line spectroscopic databases, such as HITRAN[40] and GEISA,[41] with accurate *ab initio* line shape parameters. This is a very promising direction since the theoretical calculations can cover temperature and spectral ranges that are very challenging to access experimentally. Furthermore, the *ab initio* calculations give direct access to all the beyond-Voigt line shape parameters, while experimentally, it is often difficult to disentangle contributions of different line shape effects from the fits to measured spectra. This gives important input to the community discussion on the physical meaning of the complex Dicke parameter and its relevance for atmospheric spectra. Previous fully *ab initio* calculations of the complex Dicke parameter were done for simpler systems of an atom-perturbed[42–52] and self-perturbed hydrogen molecule.[53,54] Recently, the complex Dicke parameter has been calculated for some N_2-

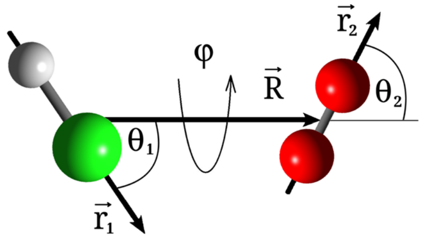

FIG. 1. Coordinates used to describe the HCl–O_2 interaction. See the text for details.

perturbed CO lines.[55] In the case of molecular systems relevant to the Earth's atmosphere, the complex Dicke parameter has been mainly determined from the phenomenological fits to experimental spectra, and in these cases, the physical interpretation of its value is questionable. In particular, in this work, we show that the value of the real part of the complex Dicke parameter that was obtained from the fit to experimental spectra[25] (for the case of the line considered in this article) is almost three times larger than its best estimate.

This paper is organized as follows. In Sec. II, we report the *ab initio* PES for the HCl($X^1\Sigma^+$)–O_2($X^3\Sigma_g^-$) system used in the line shape calculations. We discuss the computational methodology behind this PES, as well as its topography and basic characteristics, and we further decompose the PES into angle-dependent and radial parts. The latter are used in the quantum scattering calculations, the details of which are described in Sec. III. There, we discuss our methodology of setting up and numerically solving the close-coupling equations whose solutions allow us to obtain the relevant *S*-matrix elements from the appropriate scattering boundary conditions and to determine the generalized spectroscopic cross sections (GSXSs). We report the results of our calculations, and we discuss the collision simulation parameters as well as the method of constructing the expansion basis for the close-coupling wave functions used by us in the computations. Section IV contains the details and the results of the calculations of line shape parameters for the R(0) 0–0 ground-vibrational transition in the $H^{35}Cl$ isotopomer perturbed by O_2 and the comparison of our results with the available experimental data. Finally, we conclude the present investigation in Sec. V where we summarize our results and put them in perspective of future work.

II. POTENTIAL ENERGY SURFACE

As depicted in Fig. 1, the coordinates used to represent the four-dimensional (4D) HCl–O_2 PES are the Jacobi coordinates R, θ_1, θ_2, and φ. $\vec{R}$ is the vector between the centers of mass of the two fragments, and $\vec{r}_1$ and $\vec{r}_2$ are vectors aligned with each molecule. Coordinate R is the length of vector $\vec{R}$, while coordinates θ_1 and θ_2 represent (respectively) the angles between $\vec{R}$ and the vectors $\vec{r}_1$ and $\vec{r}_2$. The fourth coordinate is the dihedral (out of plane) torsional angle, labeled φ, which is the angle between the vectors $\vec{R} \times \vec{r}_1$ and $\vec{R} \times \vec{r}_2$. Note that for $\theta_1 = 0°$, the HCl molecule aligns with the Cl atom pointing to the center-of-mass of the O_2 molecule.

A. Electronic structure calculations

For construction of the PES, both monomers were held rigid. The bond distances for HCl and O_2 were fixed at their ground rovibrational state vibrationally averaged bond distances, r_{HCl} = 1.283 87 Å and r_{OO} = 1.207 52 Å, respectively, consistent with their experimental rotational constants.

The final high-level PES was computed using explicitly correlated unrestricted coupled-cluster theory[56] (UCCSD(T)-F12b). The complete basis set limit was estimated by extrapolating calculations at the UCCSD(T)-F12b/VTZ-F12 and UCCSD(T)-F12b/VQZ-F12 levels[57] using the l^{-3} formula.[58] All *ab initio* calculations were performed using the Molpro electronic structure code package.[59] To ensure convergence to the desired triplet electron configuration, the restricted open-shell Hartree–Fock (roHF) reference was obtained by first using MOLPRO's CASSCF (multi) algorithm with the occupation of the desired configuration specified, followed by a single iteration of the roHF SCF algorithm to prepare the orbitals for the UCCSD(T)-F12b procedure. To avoid placing expensive high-level data in energetically inaccessible regions, a lower-level guide surface was first constructed. This was done using similarly computed data, but at the reduced UCCSD(T)-F12b/VDZ-F12 level of theory. Exploiting the system's symmetry, energies were only computed in the reduced angular range: $0 < \theta_1 < 180°$, $0 < \theta_2 < 90°$, and $0 < \varphi < 180°$.

B. Analytical representation and characterization of the PES

As we have done in the past for other vdW dimers composed of linear monomers,[60–63] the PES analytical representation was constructed using an automated interpolating moving least squares (IMLS) methodology, freely available as a software package under the name AUTOSURF.[64] As usual,[65,66] a local fit was expanded about each data point, and the final potential is obtained as the normalized weighted sum of the local fits. This interpolative approach can accommodate arbitrary energy-surface topographies, being particularly advantageous in systems with large anisotropy. The fitting basis and most other aspects of the IMLS procedure were similar to those for other previously treated systems that have been described in detail elsewhere.[64,66,67]

The shortest intermonomer center-of-mass distance considered is R = 2.3 Å. The short-range part of the PES is restricted by excluding regions with repulsive energies above a maximum of 8 kcal/mol (~2 800 cm^{-1}) relative to the separated monomer asymptote. The *ab initio* data coverage in the fitted PES extends to R = 20 Å, while the zero of energy is set at infinite center-of-mass separation between the monomers.

For the high-level PES, the global estimated root-mean-squared fitting error tolerance was set to 0.64 cm^{-1}, and the total number of automatically generated symmetry-unique points needed to reach that target was 2452 (the final estimated error is 0.09 cm^{-1} for energies below the asymptote). To guide the placement of high-level data, a lower-level guide surface was constructed using 2000 symmetry-unique points, distributed using a Sobol sequence[68] biased to sample the short range region more densely. The analytical representation of the PES is available from the authors upon request.

Figure 2 shows a 2D representation of the PES (denoted as R-optimized) as a function of the extended angles $\tilde{\theta}_1$ and $\tilde{\theta}_2$ for planar

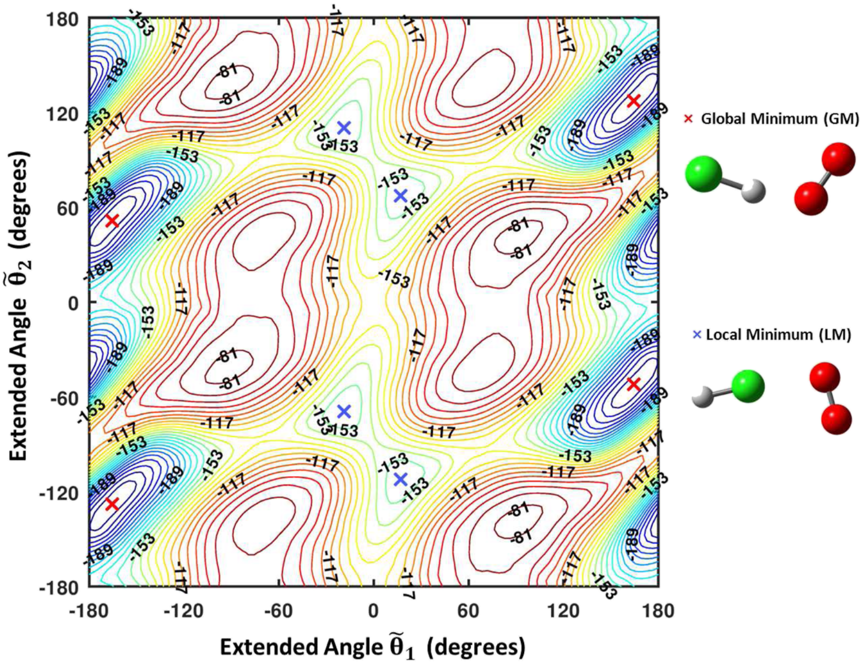

FIG. 2. *R*-optimized contour plot of the PES as a function of the extended angles $\tilde{\theta}_1$ and $\tilde{\theta}_2$ for planar configurations (φ = 0° or 180°). For each pair of angles, the energy (given in cm^{-1}) is optimized with respect to the center-of-mass distance *R*.

configurations. The extended-angle coordinates have been described in detail elsewhere.[69] For planar geometries ($\varphi = 0$ for quadrants II and IV and $\varphi = 180$ for quadrants I and III), the plot describes the complete ranges of $\tilde{\theta}_1$ and $\tilde{\theta}_2$, relaxing the intermonomer distance coordinate r_0 for each pair of angles. This type of plot provides unique insights into the isomers in the system since for many systems—those (such as this one) without non-planar minima—the plot will include all isomers and any planar isomerization paths between them, making it easy to visualize planar motions during which φ changes from 0 to 180. There are two equivalent local minima (LM) and two equivalent global minima (GM) in the PES, each duplicated and appearing twice in the extended angles plot, which shows four wells of each type.

The geometric parameters of the two isomeric planar structures are given in Table I, and their images are provided with Fig. 2. Both types of minima can be described as skewed-T-shaped. The GM, with a well-depth of 223.47 cm^{-1}, finds the H-atom of HCl pointed nearly directly toward the O_2 molecule (θ_1 = 162.1°), while the O_2 molecule is rotated significantly from side-on (θ_2 = 124.2°), bringing one of the O-atoms closer to the H-atom. The LM, with a well-depth of 157.52 cm^{-1}, is similar, but with the Cl-atom of HCl pointing toward the O_2 molecule, which is also rotated to bring an O-atom closer to the Cl-atom, but in the case of LM, less rotation from side-on is needed to maximize the interaction. Beginning at one of the LM, a conrotatory motion of the two monomers provides a very facile path to the other, symmetry-equivalent LM. A somewhat larger barrier separates LM and GM along a disrotatory path.

TABLE I. Geometric parameters and potential energy for stable structures in the PES. Energies are given relative to the asymptote. Units are angströms, degrees, and cm^{-1}.

	GM	LM
R	3.952	3.541
θ_1	162.1	18.1
θ_2	124.2	68.0
φ	180	180
V	−223.47	−157.52

Figure 3 shows radial cuts through the PES for eight different angular poses. The points represent *ab initio* data (not included in the fit), while the lines plot the fitted PES. This helps one appreciate the anisotropy of the PES as reflected in the different values of *R* at which the onset of a steep repulsive wall begins, as well as the accuracy of the fit as the lines pass through the data points.

C. Decomposition of the PES

The four-dimensional PES is prepared for scattering calculations by projecting over the set of bispherical harmonics,

$$V(R,\theta_1,\theta_2,\varphi) = \sum_{L_1,L_2,L} A_{L_1L_2L}(R) I_{L_1L_2L}(\theta_1,\theta_2,\varphi), \tag{1}$$

where L_1 and L_2 are non-negative quantum numbers and L satisfies the triangle inequality $|L_1 - L_2| \leq L \leq L_1 + L_2$. Additionally, L_2 can

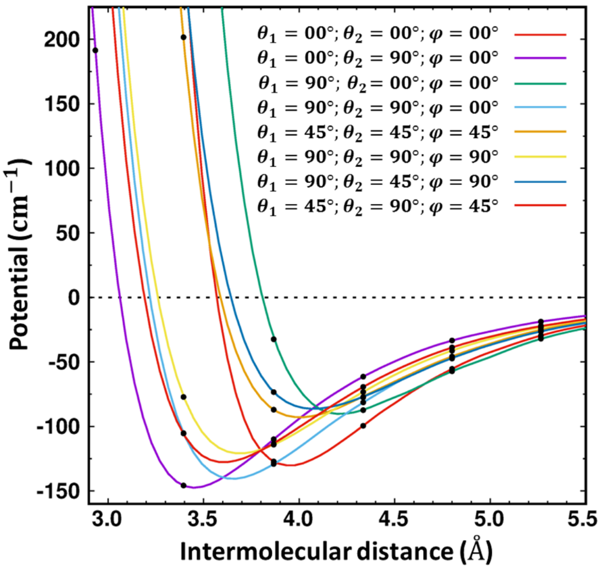

FIG. 3. Various radial cuts defined by different orientational poses of the monomers. In all cases, energies are in cm^{-1}, lines represent the fitted PES, and points represent *ab initio* calculations (not used in the fit).

take only even values due to the symmetry of the O_2 molecule and $L_1 + L_2 + L$ must be an even integer.[70] The bispherical harmonics are defined as[71]

$$I_{L_1L_2L}(\theta_1,\theta_2,\varphi=\varphi_1-\varphi_2) = \sqrt{\frac{2L+1}{4\pi}}\sum_m C^{L_1L_2L}_{m-m0} \times Y_{L_1m}(\theta_1,\varphi_1)Y_{L_2-m}(\theta_2,\varphi_2), \qquad (2)$$

where $Y_{L_im}(\theta_i,\varphi_i)$ denotes the usual spherical harmonics for each molecule and $C^{L_1L_2L}_{m-m0}$ is the Clebsch–Gordan coefficient. $A_{L_1L_2L}(R)$ is the radial term, which can be obtained by integrating Eq. (1) over the angular distribution,[70,72]

$$A_{L_1L_2L}(R) = \frac{8\pi^2}{2L+1}\int_0^{2\pi}d\varphi\int_0^{\pi}\sin\theta_1\,d\theta_1\int_0^{\pi}\sin\theta_2\,d\theta_2 \times V(R,\theta_1,\theta_2,\varphi)I_{L_1L_2L}(\theta_1,\theta_2,\varphi). \qquad (3)$$

The PES was prepared as the set of 271 radial terms with the maximum $(L_1, L_2, L) = (10, 10, 20)$. The calculations were performed on the radial grid of 1001 points, from 2.6 to 28.6 Å. Figure 4 shows the comparison between the dominating isotropic radial term A_{000} and several anisotropic contributions. The radial coefficients allow us to express the PES as the potential matrix, whose elements are used in the close-coupling equations; see Eq. (21) in Ref. 72.

III. QUANTUM SCATTERING CALCULATIONS

We perform quantum scattering calculations in the body-fixed (BF) frame of reference, following the formalism introduced by Launay[73] and extensively elaborated upon by Alexander and DePristo.[74] The scattering wavefunction is expanded in a complete set of eigenfunctions of $\hat{\mathbf{N}}_{12}^2$, $|\hat{N}_{12_{Z'}}|$, $\hat{\mathbf{J}}^2$, $\hat{J}_Z$, and $\hat{\Pi}$,

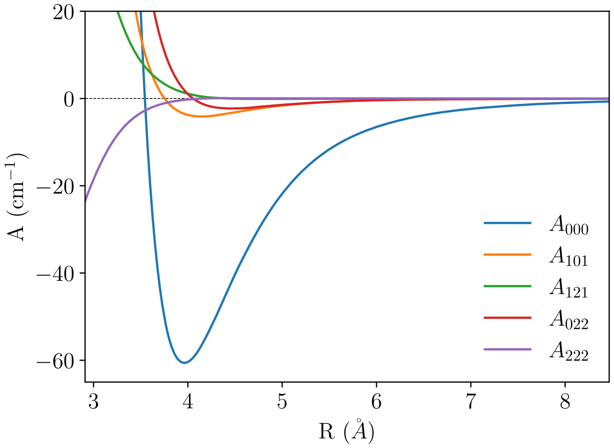

FIG. 4. The comparison between the isotropic radial term (blue line) and largest anisotropic contributions. Note that the radial terms are shown divided by the normalization factor $8\pi^2/(2L+1)$.

$$|(N_1N_2)N_{12}\bar{\Omega}JM\epsilon\rangle = \frac{1}{\sqrt{2(1+\epsilon p\delta_{\bar{\Omega},0})}}\big(|(N_1N_2)N_{12}\bar{\Omega}JM\rangle + \epsilon p|(N_1N_2)N_{12}-\bar{\Omega}JM\rangle\big), \qquad (4)$$

where

$$|(N_1N_2)N_{12}\Omega JM\rangle = |(N_1N_2)N_{12}\Omega\rangle|JM\Omega\rangle \qquad (5)$$

and $\hat{\mathbf{J}}$ is the total angular momentum, $\hat{J}_Z$ is its projection on the space-fixed Z axis, and $\hat{\Pi}$ is the parity operator. $\hat{\mathbf{N}}_{12}$ is an angular momentum resulting from the coupling of the rotational angular momenta of HCl ($\hat{\mathbf{N}}_1$) and O_2 ($\hat{\mathbf{N}}_2$), and $\hat{N}_{12_{Z'}}$ is the projection of $\hat{\mathbf{N}}_{12}$ on the body-fixed (intermolecular) Z' axis with the direction determined by the centers of mass of the molecules. Here, $\bar{\Omega} = |\Omega|$ denotes an absolute value of a given eigenvalue of $\hat{N}_{12_{Z'}}$, ϵ is the spatial parity of the system, $p = (-1)^{N_1+N_2+J-N_{12}}$, and $\bar{\Omega} \in \langle 0, \min(N_{12}, J)\rangle$. J is the total angular momentum quantum number associated with the eigenvalue of $\hat{\mathbf{J}}^2$. M denotes the eigenvalue of $\hat{J}_Z$. The eigenfunctions of $\hat{\mathbf{J}}^2$, $\hat{J}_Z$, $\hat{\mathbf{N}}_{12}$, and $\hat{N}_{12_{Z'}}$ are products of the eigenfunctions of $\hat{\mathbf{N}}_{12}$, and $\hat{N}_{12_{Z'}}$ ($|(N_1N_2)N_{12}\Omega\rangle$) and symmetric-top eigenfunctions

$$\langle\Theta,\Phi,\chi|JM\Omega\rangle = \sqrt{\frac{2J+1}{4\pi}}D^{J\,*}_{M\Omega}(\Theta,\Phi,0), \qquad (6)$$

defined using Wigner rotation matrix, D, and Euler angles (Θ, Φ, χ) describing a transformation between the space-fixed (SF) and body-fixed frames. Note that the basis vectors commonly used in calculations performed in the SF framed are related to basis vectors defined in Eq. (4) through a transformation

$$|(N_1N_2)N_{12}LJM\epsilon\rangle = (-1)^{-N_{12}+L}\sum_{\bar{\Omega}}(-1)^{\bar{\Omega}}\sqrt{\frac{2(2L+1)}{(1+\epsilon p\delta_{\bar{\Omega},0})}} \times \begin{pmatrix} N_{12} & L & J \\ \bar{\Omega} & 0 & -\bar{\Omega} \end{pmatrix}|(N_1N_2)N_{12}\bar{\Omega}JM\epsilon\rangle. \quad (7)$$

L is the quantum number labeling the eigenvalues of the $\hat{\mathbf{L}}^2$ operator for the squared orbital angular momentum of relative motion of HCl and O_2.

The scattering wavefunction of the system is expanded in the basis set introduced in Eq. (4),

$$|\Psi\rangle = \sum_{\substack{J,M,\epsilon,N_1,\\N_2,N_{12},\bar{\Omega}}}|(N_1N_2)N_{12}\bar{\Omega}JM\epsilon\rangle\frac{f^{JM\epsilon}_{N_1,N_2,N_{12},\bar{\Omega}}(R)}{R}. \quad (8)$$

Substituting this expansion to the Schrödinger equation for the scattering system involving two rigid diatomic molecules in $^1\Sigma$ electronic states leads to a set of coupled equations on coefficients $f^{J\epsilon}_{\gamma}(R)$,

$$\frac{d^2}{dR^2}f^{J\epsilon}_{\gamma}(R) = \sum_{\gamma'}W^{J\epsilon}_{\gamma,\gamma'}(R)f^{J\epsilon}_{\gamma'}(R), \quad (9)$$

where we introduced a shorthand notation for $\gamma = \{N_1, N_2, N_{12}, \bar{\Omega}\}$. Since $\hat{\mathbf{J}}^2$, $\hat{J}_Z$, and $\hat{\Pi}$ commute with the scattering Hamiltonian, J, M, and ϵ are conserved during the collision, and coupled equations can be solved for each J, M, and ϵ block independently. Additionally, in the absence of external fields, the equations are independent of M, and this index is suppressed in Eq. (9). The coupling matrix

$$W^{J\epsilon}_{\gamma,\gamma'}(R) = 2\mu V^{J\epsilon}_{\gamma,\gamma'}(R) + \frac{1}{R^2}\hat{\mathbf{L}}^{2\,J\epsilon}_{\gamma,\gamma'} - \delta_{\gamma,\gamma'}k^2_{\gamma} \quad (10)$$

involves contributions from the HCl–O_2 potential energy surface, $V^{J\epsilon}_{\gamma,\gamma'}(R)$, the relative motion of O_2 with respect to HCl, quantified by the square relative angular momentum operator, $\hat{\mathbf{L}}^{2\,J\epsilon}_{\gamma,\gamma'}$, and the relative kinetic energy of the colliding pair, expressed using the wavevector $k_{\gamma} = \sqrt{2\mu(E - E_{N_1} - E_{N_2})}$. Here, E is the total energy of the scattering system, and E_{N_i} denotes the internal (rotational) energy of the ith molecule. We assume that both molecules are in their ground vibrational states.

Table II gathers values of rotational levels of both monomers used in scattering calculations. The energy levels of the $H^{35}Cl$ molecule were calculated by solving the nuclear Schrödinger equation in the Born–Oppenheimer approximation for an isolated HCl molecule using the finite basis discrete variable representation method[75] and the potential energy curve reported by Coxon and Hajigeorgiou.[76] We neglect the hyperfine structure of rotational levels in HCl.[77] The purely rotational energies of the O_2 monomer were calculated using

$$E_{N_2} = BN_2(N_2+1) - D[N_2(N_2+1)]^2 + H[N_2(N_2+1)]^3, \quad (11)$$

where B is the rotational constant and D and H denote the first- and second-order centrifugal distortion corrections to the energy of a rigid rotor. Here, we neglect the fine-structure splitting in ground-electronic O_2 originating mostly from spin-spin interactions since it is much lower than the collision energies considered in this work. For the rotational constants in Eq. (11), we use the values reported by Hajigeorgiou:[78] $B = 1.437\,674\,521$ cm^{-1}, $D = 4.839\,482 \times 10^{-6}$ cm^{-1}, and $H = -4.220\,376 \times 10^{-14}$ cm^{-1} (only the first few digits matter for our quantum-scattering calculations, but for consistency with previous literature, we quote here the full accuracy).

The coupling matrix [Eq. (10)] has (for a given J and ϵ) almost a block-diagonal structure: the contribution from the HCl–O_2 PES is diagonal with respect to $\bar{\Omega}$, but $\bar{\Omega}' = \bar{\Omega} \pm 1$ blocks are coupled by the $\hat{\mathbf{L}}^2$ operator (see Fig. 3 in Ref. 79 and Appendix 2 in Ref. 73). The sparse structure of the matrix enables a significant reduction in computational time and memory requirements.

The coupled equations are solved in the BF frame using renormalized Numerov's algorithm[80] implemented in the BIGOS code.[81] $f^{J\epsilon}_{\gamma}(R)$ is transformed to the SF frame of reference at a sufficiently large value of R. By imposing boundary conditions on the scattering wave functions, we can derive the scattering S-matrix elements,[73] which are necessary to obtain the complex generalized spectroscopic cross sections, σ^q_{λ}. The generalized spectroscopic cross sections describe how the shape of molecular resonance is perturbed by collisions. For the isolated spectral transition $N_i \rightarrow N_f$ of rank q in a diatomic molecule perturbed by collisions with a diatomic perturber in the state N_2, the generalized cross sections are given as[82,83]

$$\sigma^q_{\lambda}(N_i, N_f, N_2, E_{\text{kin}}) = \frac{\pi}{k^2}\sum_{N'_2}\sum_{L,L',\bar{L},\bar{L}'}\sum_{J,N_{12},N'_{12}}\sum_{\bar{J},\bar{N}_{12},\bar{N}'_{12}} i^{L-L'-\bar{L}+\bar{L}'}(-1)^{\lambda+N_2-N'_2+L-L'-\bar{L}+\bar{L}'}[J][\bar{J}]\sqrt{[L][L'][\bar{L}][\bar{L}'][N_{12}][N'_{12}][\bar{N}_{12}][\bar{N}'_{12}]}$$
$$\times\begin{pmatrix} L & \bar{L} & \lambda \\ 0 & 0 & 0 \end{pmatrix}\begin{pmatrix} L' & \bar{L}' & \lambda \\ 0 & 0 & 0 \end{pmatrix}\begin{Bmatrix} q & N'_{12} & \bar{j}'_{12} \\ N'_2 & N_f & N_i \end{Bmatrix}\begin{Bmatrix} q & \bar{N}_{12} & N_{12} \\ N_2 & N_i & N_f \end{Bmatrix}\begin{bmatrix} N_{12} & N'_{12} & \bar{L} & \bar{L}' \\ \bar{N}_{12} & L & \bar{N}'_{12} & L' \\ q & \bar{J} & J & \lambda \end{bmatrix}$$
$$\times\left(\delta_{N_2N_{12}\bar{N}_{12}L\bar{L},N'_2N'_{12}\bar{N}'_{12}L'\bar{L}'} - \langle(N_iN_2)N_{12}L|S^J(E_{T_i})|(N_iN'_2)N'_{12}L'\rangle\langle(N_fN_2)\bar{N}_{12}\bar{L}|S^{\bar{J}}(E_{T_f})|(N_fN'_2)\bar{N}'_{12}\bar{L}'\rangle^*\right), \quad (12)$$

TABLE II. $H^{35}Cl$ and O_2 rotational energy levels in cm^{-1} used in our calculations of the generalized spectroscopic cross sections.

HCl		O_2	
N_1	E_{N_1}	N_2	E_{N_2}
0	0.000 000	1	2.875 330
1	20.878 402	3	17.251 397
2	62.622 535	5	43.125 880
3	125.207 074	7	80.494 597
4	208.594 056	9	129.351 507
5	312.732 923	11	189.688 714
6	437.560 568	13	261.496 460
7	583.001 390	15	344.763 133

TABLE III. Coefficients of the power-law fits to the PBXS and RDXS (see the corresponding dashed lines in Fig. 5). The coefficients are reported for every rotational state of the perturbed from $N_2 = 1$ to 11.

	PBXS		RDXS	
N_2	A (Å^2)	b	A (Å^2)	b
1	131.39	0.310	129.44	0.277
3	129.34	0.303	128.58	0.275
5	125.31	0.289	125.97	0.265
7	120.87	0.283	122.36	0.257
9	113.85	0.269	118.43	0.253
11	111.82	0.280	116.60	0.254

where $[x] = 2x + 1$ and $\delta_{a\ldots z,a'\ldots z'} = \delta_{aa'}\ldots\delta_{zz'}$ and the quantities $(\cdots)$, $\{\cdots\}$, and $[\cdots]$ are Wigner 3-j, 6-j, and 12-j symbols, respectively.[84] For $\lambda = 0$, the real and imaginary parts of this cross section describe pressure broadening and pressure shift of the spectral line, respectively.[85,86] For $\lambda = 1$, the complex cross section describes the collisional perturbation of the translational motion of the molecule, which undergoes a spectral transition and is crucial in a proper description of the Dicke effect[82,87] and other effects related to the velocity-changing collisions, such as a reduction of inhomogeneous collisional broadening and asymmetry.[88] The angular momenta are coupled in the following order:

$$\hat{\mathbf{N}}_i + \hat{\mathbf{N}}_2 = \hat{\mathbf{N}}_{12}, \hat{\mathbf{N}}_f + \hat{\mathbf{N}}_2 = \hat{\hat{\mathbf{N}}}_{12},$$
$$\hat{\mathbf{N}}_i + \hat{\mathbf{N}}_2' = \hat{\mathbf{N}}_{12}', \hat{\mathbf{N}}_f + \hat{\mathbf{N}}_2' = \hat{\hat{\mathbf{N}}}_{12}',$$
$$\hat{\mathbf{N}}_{12} + \hat{\mathbf{L}} = \hat{\mathbf{J}}, \hat{\hat{\mathbf{N}}}_{12} + \hat{\hat{\mathbf{L}}} = \hat{\hat{\mathbf{J}}},$$
$$\hat{\mathbf{N}}_{12}' + \hat{\mathbf{L}}' = \hat{\mathbf{J}}, \hat{\hat{\mathbf{N}}}_{12}' + \hat{\hat{\mathbf{L}}}' = \hat{\hat{\mathbf{J}}},$$

where the non-primed and primed symbols correspond to pre- and post-collisional operators (or quantum numbers). Note that Eq. (12) implies that two distinct scattering S-matrices are needed to obtain σ_λ^q for given kinetic energy, E_{kin}. The first matrix is computed at the total energy $E_{T_i} = E_{\text{kin}} + E_{N_i} + E_{N_2}$, and the second matrix is calculated at $E_{T_f} = E_{\text{kin}} + E_{N_f} + E_{N_2}$. For the R(0) line in HCl considered in this work, $N_i = 0$, $N_f = 1$, and $q = 1$.

We made a huge effort to ensure the convergence of σ_λ^q with respect to the rotational basis set, the range of R values used to solve the coupled equations, the step of the Numerov propagator, and the number of partial waves (or, equivalently, total angular momenta J and $\bar{J}$) contributing to the sums in Eq. (12). Ultimately, the coupled equations are solved from $R_{\min} = 5a_0$ to $R_{\max} = 45a_0$. The number of steps per half-de Broglie wavelength of the scattering system varied between 15 and 30 depending on the total energy and the total angular momentum to ensure unitary of S-matrices. Additionally, the number of steps was corrected for the depth of the isotropic part of the PES (~107.4 cm^{-1}). The sums over J (and $\bar{J}$) were truncated after four consecutive J (and $\bar{J}$) blocks that contributed less than 10^{-4} Å^2 to the largest elastic state-to-state cross section at a given total energy.

In all calculations, the basis set involved all energetically accessible (open) rotational levels of the colliding pair and a certain number of energetically inaccessible (closed) levels to ensure convergence of the generalized cross sections at the level of 1%. In particular, for kinetic energies lower than 250 cm^{-1}, the basis involved 36 energy levels (up to $N_{1_{\max}} = 6$, $N_{2_{\max}} = 7$). For higher kinetic energies, the size of the basis was gradually increased, reaching 47 rotational levels of the colliding pair at $E_{\text{kin}} = 425$ cm^{-1}.

Figure 5 shows the calculated dependencies of pressure broadening (PBXS), $\text{Re}\left[\sigma_0^1(E_{\text{kin}})\right]$, pressure shift (PSXS), $\text{Im}\left[\sigma_0^1(E_{\text{kin}})\right]$, and Dicke cross sections (RDXSs for $\text{Re}\left[\sigma_1^1(E_{\text{kin}})\right]$ and IDXS for $\text{Im}\left[\sigma_1^1(E_{\text{kin}})\right]$) on the collision kinetic energy for various rotational states of the perturber, N_2. The solid lines come from our *ab initio* calculations, and the dashed lines are extrapolations. The real (PBXS and RDXS) and imaginary (PSXS and IDXS) parts of the generalized cross sections as a function of kinetic energy exhibit very different behavior; therefore, we discuss them separately in the two following paragraphs.

The PBXS and RDXS as a function of kinetic energy exhibit a power-law behavior. We use this property to extrapolate the *ab initio* cross sections to higher energies,

$$\text{Re}\left[\sigma_\lambda^1(E_{\text{kin}})\right] = A\left(\frac{E_0}{E_{\text{kin}}}\right)^b, \tag{13}$$

where $E_0 = 100$ cm^{-1} is a reference kinetic energy. The fit coefficients, A and b, are determined for each rotational level and are given in Table III. The PBXS and RDXS become almost state-independent for larger N_2 (such behavior of the PBXS has already been observed for other systems, such as CO–O_2,[61] CO–N_2,[70] O_2–N_2,[72] N_2–H_2,[89] and N_2–N_2[90]). We use this property to extrapolate the PBXS and RDXS for $N_2 > 11$ (for $N_2 > 11$, we assume the same value as for $N_2 = 11$). We discuss the estimations of the uncertainties caused by the extrapolations in Sec. IV.

The imaginary parts of the cross sections, i.e., the PSXS and IDXS, reveal very different features from their real counterparts. First, they are much more demanding in terms of converging the quantum-scattering calculations (i.e., they require a much larger basis, larger integration range, etc., compared to the PBXS and RDXS). Second, their dependencies on the kinetic energy and N_2 are much less predictable and, hence, more difficult to extrapolate; see the right upper and lower panels in Fig. 5. Due to a lack of

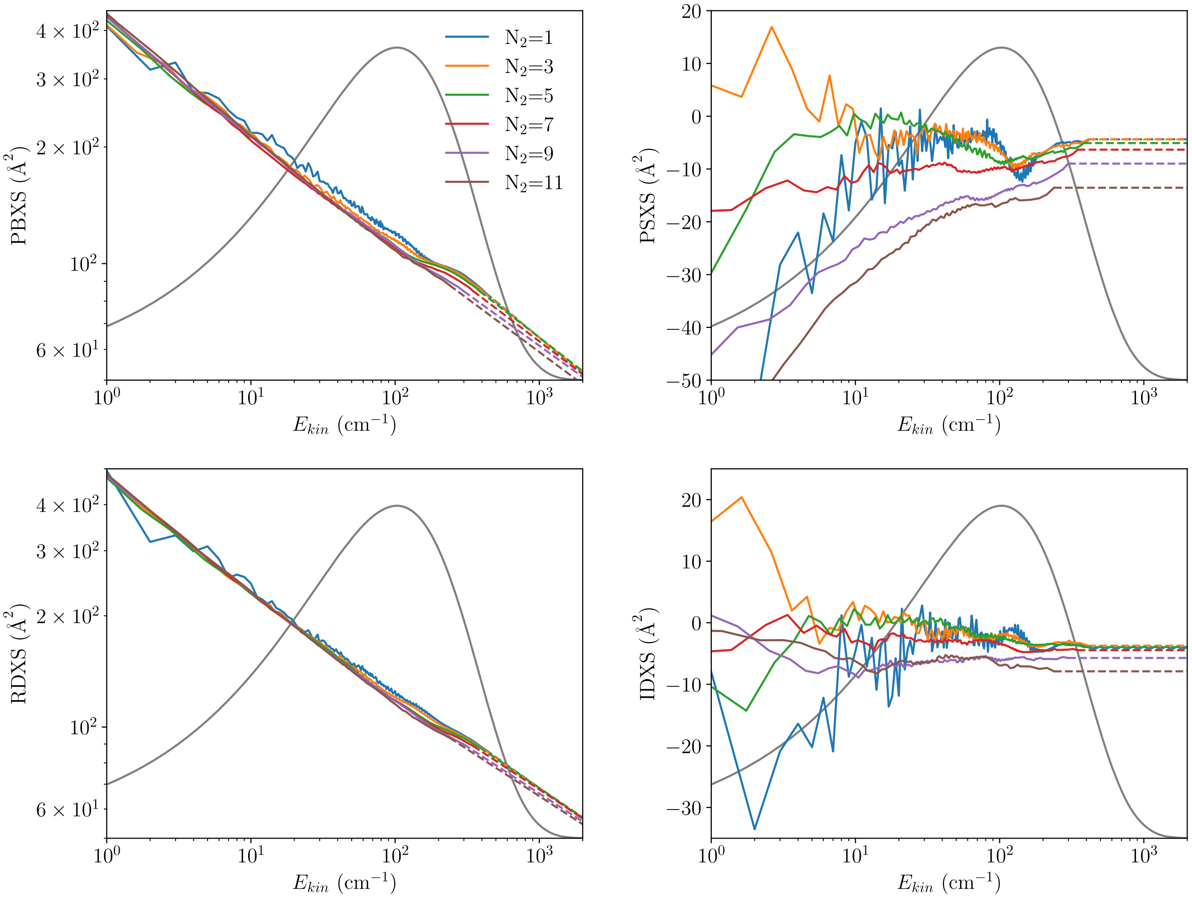

FIG. 5. Generalized spectroscopic cross sections as a function of relative kinetic energy, E_{kin}, for the first six rotational states (N_2 = 1 to 11) of the perturber molecule (i.e., oxygen molecule). The left and right upper panels correspond to pressure broadening and shift (γ_0 and δ_0), and the left and right lower panels correspond to the real and imaginary parts of the complex Dicke parameter ($\tilde{\nu}^r_{opt}$ and $\tilde{\nu}^i_{opt}$). The solid lines are the results of our *ab initio* calculations, and the dashed lines are the extrapolations (see the text for details). As a reference, we plot the Boltzmann E_{kin} distribution at T = 296 K as a gray curve (note that for the Boltzmann distribution in all the panels, the vertical axis is linear and has an arbitrary unit).

more accurate information, we extrapolate PSXS and IDXS to higher energies simply with horizontal lines (see Fig. 5) and assume the same value as for $N_2 = 11$ for $N_2 > 11$. On one hand, these crude extrapolations for PSXS and IDXS inherently induce much larger relative uncertainties compared to the PBXS and RDXS. On the other hand, the magnitudes of PSXS and IDXS are much smaller than PBXS; hence, these large relative uncertainties of PSXS and IDXS have small impact on the collision-induced shapes of the HCl line. We provide a detailed discussion of the uncertainties in Sec. IV.

IV. COLLISION-INDUCED LINE SHAPE PARAMETERS

The speed-dependent spectroscopic parameters, pressure broadening and shift, $\gamma(v)$ and $\delta(v)$, can be obtained from the generalized spectroscopic cross section, Eq. (12), from the following integral:[53,91]

$$\begin{aligned}\gamma(v) - i\delta(v) &= \frac{1}{2\pi c}\frac{1}{k_B T}\frac{2v_p^2}{\sqrt{\pi}v}e^{-\frac{v^2}{v_p^2}}\sum_{N_2} p_{N_2}\\ &\quad\times\int_0^\infty \mathrm{d}x\, x^2 e^{-x^2}\sinh\left(\frac{2vx}{v_p}\right)\\ &\quad\times\sigma_0^1(N_i = 0, N_f = 1, N_2, E_{\mathrm{kin}} = \mu x^2 v_p^2/2), \qquad (14)\end{aligned}$$

where v is a given speed of the active molecule, $v_p = \sqrt{2k_B T/m_2}$ is the most probable perturber speed, v_r is the relative absorber–perturber speed, and $x = v_r/v_p$. N_i and N_f denote, respectively, the initial and final rotational quantum numbers of the active molecule. k_B is the Boltzmann constant, and c is the speed of light in vacuum. The statistical weight p_{N_2} denotes the population of the N_2-th rotational state of the perturbing molecule at a given temperature, T,

$$p_{N_2}(T) = \frac{1}{Z(T)}(2N_2 + 1)e^{-E_{N_2}/(k_B T)}, \qquad (15)$$

where E_{N_2} is the energy of that rotational state, and

$$Z(T) = \sum_{N_2} (2N_2 + 1) e^{-E_{N_2}/(k_B T)} \tag{16}$$

is the partition function. The summation up to $N_2 = 39$ covers over 99% of the perturber population at 296 K. The total nuclear spin of $^{16}O_2$ molecule is zero; hence, the nuclear spin statistic does not influence Eqs. (15) and (16).

The full speed dependencies of γ and δ are often too complex and inconvenient from the perspective of spectroscopic applications (including populating the HITRAN database[92,93]). Therefore, we approximate the $\gamma(v)$ and $\delta(v)$ functions on simple quadratic functions,[91,94]

$$\gamma(v) + i\delta(v) \approx \gamma_0 + i\delta_0 + (\gamma_2 + i\delta_2)\left(\frac{v^2}{v_m^2} - \frac{3}{2}\right), \tag{17}$$

where v_m is the most probable speed of the active molecules and γ_0 and δ_0 are the speed-averaged pressure broadening and shift, respectively. They are obtained[91] at given gas temperature, T, as

$$\gamma_0(T) - i\delta_0(T) = \frac{1}{2\pi c}\frac{\langle v_r \rangle}{k_B T}\sum_{N_2} p_{N_2}\int_0^\infty \mathrm{d}z\, z e^{-z} \times \sigma_0^1(N_i, N_f, N_2; E_{\mathrm{kin}} = z k_B T), \tag{18}$$

where $\langle v_r \rangle = \sqrt{8 k_B T/\pi\mu}$ is the mean relative speed of the colliding molecules. μ is their reduced mass. z is a dimensionless kinetic energy of a collision, $z = E_{\mathrm{kin}}/(k_B T)$. Note that γ_0 and δ_0 can also be obtained by averaging $\gamma(v)$ and $\delta(v)$ from Eq. (14) over the Maxwell–Boltzmann distribution of the absorber, v, at a given temperature, T. To calculate γ_2 and δ_2, we assume that the slopes of the quadratic approximation and the actual speed dependencies are equal at $v = v_m$,[53,91]

$$\frac{\mathrm{d}}{\mathrm{d}v}(\gamma(v) + i\delta(v))|_{v=v_m} = \frac{2}{v_m}(\gamma_2 + i\delta_2). \tag{19}$$

The derivative can be done analytically, which leads to the direct formulas for γ_2 and δ_2,[91,92]

$$\gamma_2(T) - i\delta_2(T) = \frac{1}{2\pi c}\frac{1}{k_B T}\frac{v_p}{\sqrt{\pi}} e^{-y^2}\sum_{N_2} p_{N_2}\int_0^\infty \mathrm{d}x \times \left[2x\cosh(2xy) - \left(\frac{1}{y} + 2y\right)\sinh(2xy)\right] \times x^2 e^{-x^2}\sigma_0^1(N_i, N_f, N_2; E_{\mathrm{kin}} = \mu x^2 v_p^2/2), \tag{20}$$

where $y = v_m/v_p$. In Fig. 6, the full speed-dependence of our *ab initio* $\gamma(v)$ and $\delta(v)$ at 296 K (black solid lines) is compared with the corresponding quadratic approximation (black dashed lines), Eq. (17), and the speed-averaged values (red dashed lines), Eq. (18).

In some experiments conducted in the high-pressure regime, where the contribution from the Gaussian component is no longer significant, the spectra are fitted with simple Lorentz profiles. However, the speed-dependence of γ and δ may be non-negligible even at high pressure. Therefore, we calculate a weighted sum of Lorentz profiles (WSLPs) for each frequency ν taking average over the Maxwell–Boltzmann distribution $f_m(\vec{v})$ of the active molecule's velocity,[95]

$$I_{\mathrm{WSLP}}(\nu - \nu_0') = \frac{1}{\pi}\int \mathrm{d}^3\vec{v}\, f_m(\vec{v})\frac{\gamma(v)}{\gamma^2(v) + (\nu - \nu_0' - \delta(v))^2}, \tag{21}$$

where ν_0' is the unperturbed line position without the pressure shift effect. By fitting a Lorentzian profile to the simulated WSLP, we obtain the effective width of the line, which is smaller than γ_0 and can be compared with experimental broadening obtained from Lorentzian fits to the measured lines. Note that the effective width of WSLP is smaller than γ_0 because the speed-dependence of γ dominates over the speed-dependence of δ (otherwise, the effective width of WSLP would be larger).

The rate of the velocity-changing collisions is quantified by the complex Dicke parameter, $\widetilde{\nu}_{opt}$, which is calculated as[42,53]

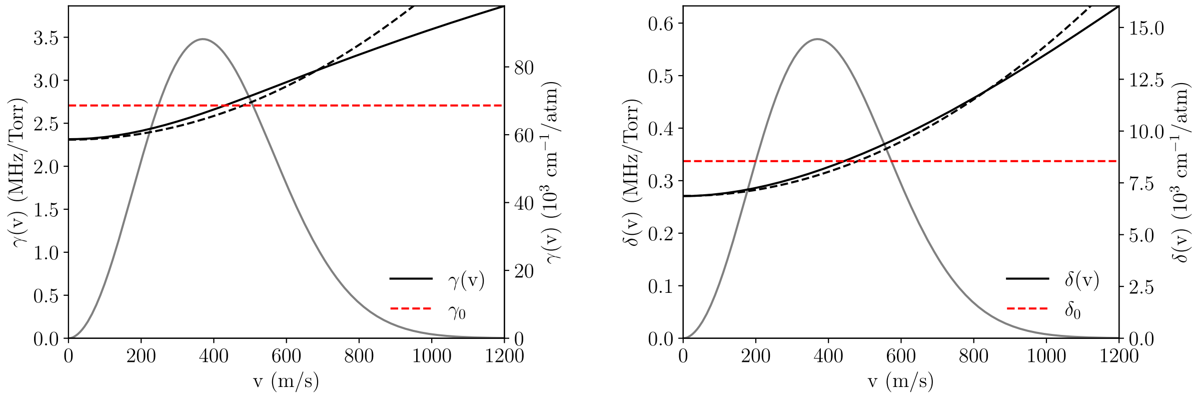

FIG. 6. *Ab initio* speed-dependent pressure broadening and shift, $\gamma(v)$ and $\delta(v)$, for the O_2-perturbed 0–0 R(0) line in the $H^{35}Cl$ molecule at 296 K, their quadratic approximation (the dashed curve), and the corresponding speed-averaged parameters γ_0 and δ_0 (the red dashed line). As a reference, the corresponding Maxwellian speed distribution of the perturber (gray solid line) at 296 K is shown in arbitrary units.

TABLE IV. Comparison between our *ab initio* line shape parameters and the available experimental data for the 0–0 R(0) line in $H^{35}Cl$ perturbed by O_2. All line shape parameters are expressed in units of MHz/Torr. *n* is a dimensionless fitted temperature exponent; see Eq. (23). The numbers in parentheses correspond, in the case of our theoretical results, to the estimated numerical uncertainty and, in the case of experimental data, to one standard deviation.

	T (K)	γ_0	δ_0	γ_2	δ_2	ν^r_{opt}	ν^i_{opt}
This work	296	2.707(41)	0.34(11)	0.2656(40)	0.044(14)	0.302(11)	−0.040(36)
This work, WSLP	296	2.691(41)					
This work	298	2.693(41)	0.34(11)	0.2636(40)	0.044(14)	0.300(11)	−0.040(36)
This work, WSLP	298	2.676(41)					
Zu *et al.* (TuFIR[a])[23]	298	2.70(5)					
Zu *et al.* (Har. mul.[b])[23]	298	2.60					
Drouin[24]	296	2.595(5)	0.280(1)				
Morino and Yamada[25]	296	2.632(15)	0.2697(37)			0.950(33)	
	T (K)	n_{γ_0}	n_{δ_0}	n_{γ_2}	n_{δ_2}	$n_{\nu^r_{\text{opt}}}$	$n_{\nu^i_{\text{opt}}}$
This work	296	0.776(21)	0.37(20)	0.837(22)	0.36(18)	0.721(45)	0.79(74)
This work, WSLP	296	0.774(21)					
Drouin[24]	296	0.79(1)	0.50(3)				

[a] A high resolution tunable far infrared spectrometer.

[b] A harmonic multiplier radiation source.

$$\begin{aligned}\text{Re}[\tilde{\nu}_{opt}(T)] - i\text{Im}[\tilde{\nu}_{opt}(T)] &= \frac{1}{2\pi c}\frac{M_2\langle v_r\rangle}{k_B T}\sum_{N_2} p_{N_2}\int_0^\infty \mathrm{d}z\, z e^{-z} \\ &\quad\times\Big[\frac{2}{3}z\sigma_1^1(N_i, N_f, N_2; E_{\text{kin}} = zk_B T) \\ &\quad - \sigma_0^1(N_i, N_f, N_2; E_{\text{kin}} = zk_B T)\Big], \end{aligned} \tag{22}$$

where $M_2 = m_2/(m_1 + m_2)$. $m_{1/2}$ is the mass of the active/perturbing molecule.

The speed-averaged coefficients were calculated for the given temperature range of 150–360 K and fitted with the power-law,

$$\gamma_0(T) = \gamma_0(T_0)\left(\frac{T_0}{T}\right)^{n_{\gamma_0}}, \tag{23}$$

where $T_0 = 296$ K is a reference temperature and n_{γ_0} is the fitted temperature exponent. Equation (23) is written for the case of the γ_0 parameter, but we use the same power-law function for other line shape parameters. The power-law coefficients are given in Table IV, where we compare them with Ref. 24.

In Fig. 7, we show a comparison of the calculated line shape parameters with experimental data. Our estimations of their total combined relative uncertainties at 296 K are 1.5% for γ_0 and γ_2, 3.5% for $\tilde{\nu}^r_{opt}$, 30% for δ_0 and δ_2, and 90% for $\tilde{\nu}^i_{opt}$. The contributions from the quantum-scattering calculations are almost negligible, i.e., 1% level for imaginary parts and much smaller uncertainty for the real parts of the cross sections. The main contributions to the total uncertainties at 296 K originate from the cross-sectional extrapolations to higher kinetic energies and higher perturber's rotational states; see the dashed lines in Fig. 5. Our estimated uncertainties are depicted in Fig. 7 as gray shadows—they decrease with the decreasing temperature because the extrapolations to higher temperatures and higher N_2 play a smaller role at lower temperatures. The much larger uncertainty for the shift and imaginary part of the complex Dicke parameter is because the dependence of the corresponding cross sections (see the right panels in Fig. 5) on kinetic energy and N_2 is more difficult to predict and, hence, to extrapolate.

However, the outcome of the uncertainty analysis, in the context of accurate spectra simulations and spectroscopic data analysis, should not be the uncertainties of the particular line shape parameters, but how they propagate on the simulated line shapes. It was shown in Ref. 51 that a 1.5% uncertainty in γ_0 results in relative root-mean-square error (RMSE) of profile residuals of 0.7% [see Eq. (A.4) in Ref. 51]. The 30% uncertainty of the δ_0 parameter may seem to be the most worrying in this context. However, to quantify its impact on the line shape, one should not consider the relative δ_0 uncertainty, but relate the absolute uncertainty of δ_0 to the width of the line (note that γ_0 is much larger than δ_0); see Eq. (A.7) in Ref. 51. It turns out that 30% uncertainty in δ_0 results in only 1.7% line shape residuals. The four other line shape parameters (γ_2, δ_2, $\tilde{\nu}^r_{opt}$, and $\tilde{\nu}^i_{opt}$) have small impacts on the line shape. Assuming statistical independence of the uncertainties of the six line shape parameters, we estimate that the total combined uncertainties of our calculations and extrapolations correspond to 2% relative RMSE residuals in the line shape at 296 K.

The calculated line shape parameters and the available experimental data are in good agreement across the investigated temperature range (see Fig. 7). In the case of the δ_0 parameter, all the experimental points lie within one combined standard uncertainty from our *ab initio* values. Despite that, at the first glance, the uncertainties of δ_0 may seem large, we recall that they should be related to the magnitude of γ_0 (rather than δ_0) to actually reflect its impact on the final collision-perturbed shape of the line.[51]

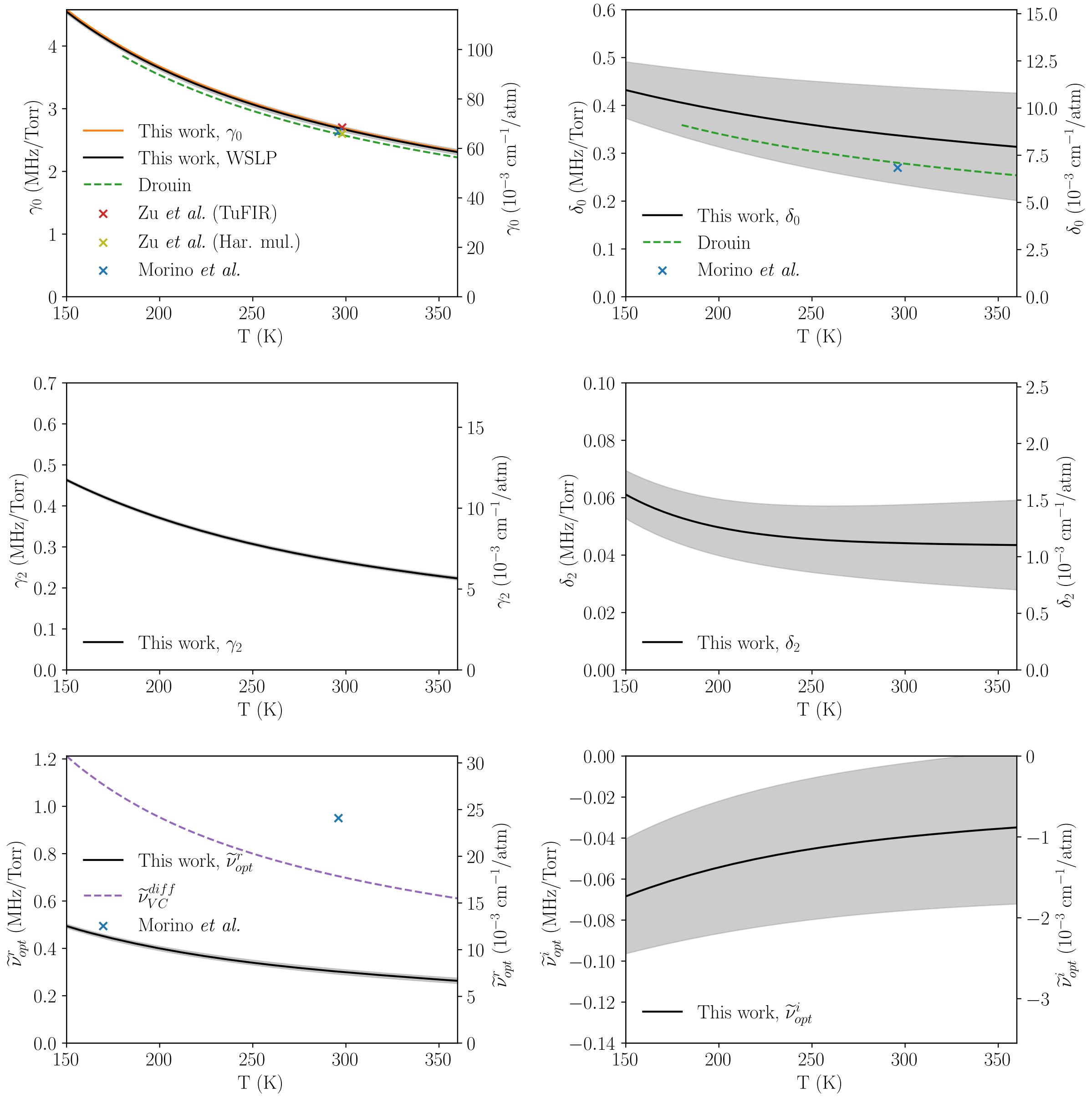

FIG. 7. Temperature dependencies of the γ_0, δ_0, γ_2, δ_2, and $\widetilde{\nu}_{opt}$ line shape parameters for the 0–0 R(0) line in $H^{35}Cl$ perturbed by O_2. Our *ab initio* results are given by black solid lines [with the effective width of the line, Eq. (21), denoted with an orange solid line]. The shaded areas correspond to the estimated numerical uncertainty of the determined line shape parameters. The experimental results[23–25] are marked with the green dashed lines and "x" symbols.

The comparison of the experimentally determined real part of the Dicke parameter, $\widetilde{\nu}^r_{opt}$, with its *ab initio* value gives a unique chance to give an important input to the long-lasting discussion on the physical meaning of the complex Dicke parameter. For the molecular systems relevant to the Earth's atmosphere, the complex Dicke parameter was determined only from phenomenological fits to experimental spectra and the physical meaning of its value is questionable. A notable exception is Ref. 55, where the authors provided values of the complex Dicke parameter for the N_2-perturbed 1-0 Q(0) line in CO (see the Appendix therein). However, this particular line is not observed in the absorption spectra of CO. It is accessible only through Raman spectroscopy, which limits its direct relevance to atmospheric studies. In this work, we show that the value of the real part of the complex Dicke parameter obtained from the fit to experimental spectra[25] for the case of the line considered in this article is almost three times larger than its actual value; see Fig. 7. This means that the line shape fits performed in Ref. 25 well reproduced the line shapes in a geometrical sense, but the underlying line shape parameters converged to unphysical values. This is caused by strong numerical correlations between the line shape parameters. The problem of retrieving unphysical values of the fitted line shape parameters is known in the literature, and it is especially pronounced for fits based on the beyond-Voigt profiles. For instance, it was reported for the case of molecular hydrogen; see Table 2 and Fig. 3 in Ref. 96 or Table 1 and Fig. 4 in Ref. 53.

Before, the complex Dicke parameter was calculated from the first principles only for simpler systems, such as atom-perturbed hydrogen molecule[48,51,52] or self-perturbed hydrogen molecule[53] (the exception is the recent work for CO–N_2[70]). For the case of molecular hydrogen, however, the contribution from inelastic collisions is so small that $\widetilde{\nu}^r_{opt}$ is very close to the frequency of the velocity-changing collisions calculated from the diffusion coefficient; see Appendix B in Ref. 42. From this perspective, the molecular hydrogen case is trivial because the simple kinetic considerations give almost the same results as the full quantum calculations of the generalized spectroscopic cross sections. In this work, we probe a very different regime where $\widetilde{\nu}^r_{opt}$ is over two times smaller than the frequency of the velocity changing collisions for HCl, $\widetilde{\nu}^{diff}_{VC}$ (see the purple dashed line in Fig. 7). Comprehensive details regarding the determination of $\widetilde{\nu}^{diff}_{VC}$ are available in the Appendix. In this case, $\widetilde{\nu}^r_{opt}$ really holds information on very nontrivial effect of correlation between a velocity-changing collision and perturbation of optical coherence associated with the considered transition.

Experimental values for γ_2, δ_2 and the imaginary part of the Dicke parameter, $\widetilde{\nu}^i_{\mathrm{opt}}$, are currently unavailable. A detailed summary of the results, which contains the room temperature coefficients, fitting parameters, and their uncertainties, can be found in Table IV. The parameters are connected with their pressure-dependent counterparts as $\Gamma_0 = \gamma_0 p$, $\Delta_0 = \delta_0 p$, $\Gamma_2 = \gamma_2 p$, $\Delta_2 = \delta_2 p$, and $\nu_{opt} = \widetilde{\nu}_{opt} p$.

V. CONCLUSION

We presented the results of the first-ever fully quantum calculations of the line shape parameters of HCl molecular resonances perturbed by a diatomic molecule. In particular, we investigated the effect of the atmospheric O_2-induced perturbations on the shape of the pure rotational R(0) transition in HCl. Using the newly calculated *ab initio* $\mathrm{HCl}(X^1\Sigma^+)$–$\mathrm{O}_2(X^3\Sigma_g^-)$ potential energy surface, we performed quantum scattering calculations using the full close-coupling approach, without making additional approximations. We used the determined *S*-matrix elements to compute the generalized spectroscopic cross sections, and we analyzed their structure using the discussed convergence and extrapolation criteria. By averaging the cross sections, we determined the temperature-dependence of the pressure broadening and shift, as well as the complex Dicke parameter for this line. This is the first *ab initio* calculation of the complex Dicke parameter done for the HCl molecule. We included the speed-dependence of the calculated line shape parameters in the analysis and obtained agreement with the available experimental data.

This study constitutes a major step toward accurate theoretical determination of the line shape parameters for molecular systems of atmospheric interest, perturbed by interactions with other air molecules. Such investigations are important for studying the intermolecular interactions between atmospheric species, as well as the interplay of different collisional effects and the discrimination between the line shape models used to recover the atmospheric information from the remote-sensed molecular spectra. These results are relevant for accurate modeling of the atmospheric spectra of HCl—the main reservoir of ozone-depleting chlorine—and for populating the spectroscopic databases (e.g., HITRAN and GEISA) with line shape parameters determined using the first principles of quantum mechanics. Furthermore, such theoretical investigations provide an independent test (as well as guidance) for the methodologies of analyzing the collisional data.

SUPPLEMENTARY MATERIAL

See the supplementary material associated with this article for the tabulated generalized spectroscopic cross sections used in the line shape calculations.

ACKNOWLEDGMENTS

A.O. and H.J. were supported by the National Science Centre in Poland through Project No. 2018/31/B/ST2/00720. M.G. was supported by the National Science Centre in Poland through Project No. 2021/43/O/ST2/00211. R.D. and E.Q.-S. were supported by the U.S. Department of Energy (Award DE-SC0019740). P.W. was supported by the National Science Centre in Poland through Project No. 2022/46/E/ST2/00282. For the purpose of Open Access, the author has applied a CC-BY public copyright licence to any Author Accepted Manuscript (AAM) version arising from this submission. We gratefully acknowledge Polish high-performance computing infrastructure PLGrid (HPC Centers: ACK Cyfronet AGH, CI TASK) for providing computer facilities and support within the computational grant, Grant No. PLG/2023/016409. Calculations have been carried out using resources provided by the Wroclaw Centre for Networking and Supercomputing (http://wcss.pl), Grant No. 546. The research is a part of the program of the National Laboratory FAMO in Toruń, Poland.

AUTHOR DECLARATIONS

Conflict of Interest

The authors have no conflicts to disclose.

Author Contributions

Artur Olejnik: Conceptualization (equal); Data curation (equal); Methodology (equal); Validation (equal); Visualization (lead); Writing – original draft (lead). **Hubert Jóźwiak**: Investigation (supporting); Software (equal); Writing – original draft (supporting);

Writing – review & editing (supporting). **Maciej Gancewski**: Validation (supporting); Writing – original draft (supporting); Writing – review & editing (supporting). **Ernesto Quintas-Sánchez**: Investigation (equal); Software (equal). **Richard Dawes**: Conceptualization (equal); Data curation (equal); Funding acquisition (supporting); Investigation (equal); Methodology (equal); Software (equal); Visualization (supporting); Writing – original draft (supporting). **Piotr Wcisło**: Conceptualization (equal); Funding acquisition (lead); Methodology (equal); Project administration (lead); Resources (lead); Supervision (lead); Validation (equal); Writing – original draft (supporting); Writing – review & editing (lead).

DATA AVAILABILITY

The data that support the findings of this study are available from the corresponding author upon reasonable request.

APPENDIX: FREQUENCY OF THE VELOCITY CHANGING COLLISIONS

In Fig. 7, we compare the real part of the Dicke parameter, $\widetilde{\nu}^{r}_{opt}$, with the frequency of the velocity changing collisions for HCl, $\widetilde{\nu}^{diff}_{VC}$. To determine this value, we employ the principle that $\widetilde{\nu}^{diff}_{VC}$ is related to the mass diffusion coefficient, D, via $\nu^{diff}_{VC} = v_m^2/(2D)$; see Appendix A in Ref. 96. We use a corresponding pressure-independent quantity as $\widetilde{\nu}^{diff}_{VC} = \nu^{diff}_{VC}/p$, where p is the pressure. The first-order approximation of the diffusion coefficient can be calculated as[97]

$$D = \frac{3}{16}\frac{(k_B T)^2}{\mu p}\frac{1}{\Omega^{(1,1)}(T)}, \tag{A1}$$

where $\Omega^{(1,1)}(T)$ is the collision integral introduced by Chapman and Cowling.[98] Here, we determine $\widetilde{\nu}^{diff}_{VC}$ by fitting the isotropic term of Eq. (1) to the Lennard-Jones (LJ) potential. We use a standard form of the LJ potential,

$$V(R) = 4\epsilon\left[\left(\frac{\sigma}{R}\right)^{12} - \left(\frac{\sigma}{R}\right)^{6}\right], \tag{A2}$$

where ϵ is the depth of the potential well and σ is the value of R for which $V(R) = 0$. The fitted LJ parameters ($\epsilon = 57.1 \pm 0.4$ cm^{-1} and $\sigma = 6.69 \pm 0.01 a_0$), along with tabulated values of the reduced collision integrals $\Omega^{(1,1)*}$ (see Tables I–M and Chapter 8.4 in Ref. 97), are then used to calculate $\Omega^{(1,1)}$.

REFERENCES

[1] R. Zander, M. R. Gunson, C. B. Farmer, C. P. Rinsland, F. W. Irion, and E. Mahieu, J. Atmos. Chem. **15**, 171 (1992).

[2] S. Solomon, Rev. Geophys. **37**, 275, https://doi.org/10.1029/1999rg900008 (1999).

[3] J. C. Farman, B. G. Gardiner, and J. D. Shanklin, Nature **315**, 207–210 (1985).

[4] L. M. Polvani, J. Keeble, A. Banerjee, R. Checa-Garcia, G. Chiodo, H. E. Rieder, and K. H. Rosenlof, Nat. Commun. **14**, 1608 (2023).

[5] P. A. Newman, L. D. Oman, A. R. Douglass, E. L. Fleming, S. M. Frith, M. M. Hurwitz, S. R. Kawa, C. H. Jackman, N. A. Krotkov, E. R. Nash, J. E. Nielsen, S. Pawson, R. S. Stolarski, and G. J. M. Velders, Atmos. Chem. Phys. **9**, 2113–2128 (2009).

[6] J. A. Mäder, J. Staehelin, T. Peter, D. Brunner, H. E. Rieder, and W. A. Stahel, Atmos. Chem. Phys. **10**, 12161–12171 (2010).

[7] S. Solomon, D. J. Ivy, D. Kinnison, M. J. Mills, R. R. Neely, and A. Schmidt, Science **353**, 269 (2016).

[8] World Meteorological Organization (WMO), Scientific assessment of ozone depletion: 2022, GAW Report No. 278, WMO, Geneva, 2022, p. 509.

[9] R. Nassar, P. F. Bernath, C. D. Boone, C. Clerbaux, P. F. Coheur, G. Dufour, L. Froidevaux, E. Mahieu, J. C. McConnell, S. D. McLeod, D. P. Murtagh, C. P. Rinsland, K. Semeniuk, R. Skelton, K. A. Walker, and R. Zander, J. Geophys. Res. **111**, D22312, https://doi.org/10.1029/2006jd007073 (2006).

[10] P. Connes, J. Connes, W. S. Benedict, and L. D. Kaplan, Astrophys. J. **147**, 1230 (1967).

[11] S. T. Ridgway, D. F. Carbon, D. N. B. Hall, and J. Jewell, Astrophys. J., Suppl. Ser. **54**, 177 (1984).

[12] J. Zmuidzinas, G. A. Blake, J. Carlstrom, J. Keene, and D. Miller, Astrophys. J. **447**, L125 (1995).

[13] M. Jura, Astrophys. J. **190**, L33 (1974).

[14] A. Dalgarno, T. de Jong, M. Oppenheimer, and J. H. Black, Astrophys. J. **192**, L37 (1974).

[15] G. Jones and W. Gordy, Phys. Rev. **136**, A1229 (1964).

[16] F. C. De Lucia, P. Helminger, and W. Gordy, Phys. Rev. A **3**, 1849 (1971).

[17] J. Pourcin and R. Romanetti, Infrared Phys. **13**, 161 (1973).

[18] J.-P. Houdeau, M. Larvor, and C. Haeusler, Can. J. Phys. **58**, 318 (1980).

[19] M. Sergent-Rozey, N. Lacome, and A. Levy, J. Mol. Spectrosc. **120**, 403 (1986).

[20] A. S. Pine and J. P. Looney, J. Mol. Spectrosc. **122**, 41 (1987).

[21] K. Park, K. V. Chance, I. G. Nolt, J. V. Radostitz, M. D. Vanek, D. A. Jennings, and K. M. Evenson, J. Mol. Spectrosc. **147**, 521 (1991).

[22] T. Klaus, S. P. Belov, and G. Winnewisser, J. Mol. Spectrosc. **187**, 109 (1998).

[23] L. Zu, P. A. Hamilton, K. V. Chance, and P. B. Davies, J. Mol. Spectrosc. **220**, 107–112 (2003).

[24] B. J. Drouin, J. Quant. Spectrosc. Radiat. Transfer **83**, 321–331 (2004).

[25] I. Morino and K. M. T. Yamada, J. Mol. Spectrosc. **233**, 77 (2005).

[26] D. Hurtmans, A. Henry, A. Valentin, and C. Boulet, J. Mol. Spectrosc. **254**, 126–136 (2009).

[27] G. Li, A. Serdyukov, M. Gisi, O. Werhahn, and V. Ebert, J. Quant. Spectrosc. Radiat. Transfer **165**, 76 (2015).

[28] D. E. Fitz and R. A. Marcus, J. Chem. Phys. **62**, 3788 (1975).

[29] H. Tran and J.-L. Domenech, J. Chem. Phys. **141**, 064313 (2014).

[30] H. Tran, J.-M. Hartmann, G. Li, and V. Ebert, J. Phys.: Conf. Ser. **810**, 012039 (2017).

[31] R. H. Dicke, Phys. Rev. **89**, 472 (1953).

[32] B. Barret, D. Hurtmans, M. R. Carleer, M. De Mazière, E. Mahieu, and P.-F. Coheur, J. Quant. Spectrosc. Radiat. Transfer **95**, 499–519 (2005).

[33] R. D. Ramachandra and T. Oka, J. Mol. Spectrosc. **122**, 16 (1987).

[34] D. H. Rank, D. P. Eastman, B. S. Rao, and T. A. Wiggins, J. Mol. Spectrosc. **10**, 34 (1963).

[35] A. S. Pine and A. Fried, J. Mol. Spectrosc. **114**, 148 (1985).

[36] W. S. Benedict, R. Herman, G. E. Moore, and S. Silverman, Can. J. Phys. **34**, 850 (1956).

[37] R. Marcus, Chem. Phys. Lett. **7**, 525 (1970).

[38] W. H. Miller, J. Chem. Phys. **53**, 1949 (1970).

[39] D. E. Fitz and R. A. Marcus, J. Chem. Phys. **59**, 4380 (1973).

[40] I. Gordon, L. Rothman, R. Hargreaves, R. Hashemi, E. Karlovets, F. Skinner, E. Conway, C. Hill, R. Kochanov, Y. Tan, P. Wcisło, A. Finenko, K. Nelson, P. Bernath, M. Birk, V. Boudon, A. Campargue, K. Chance, A. Coustenis, B. Drouin, J. Flaud, R. Gamache, J. Hodges, D. Jacquemart, E. Mlawer, A. Nikitin, V. Perevalov, M. Rotger, J. Tennyson, G. Toon, H. Tran, V. Tyuterev, E. Adkins, A. Baker, A. Barbe, E. Canè, A. Császár, A. Dudaryonok, O. Egorov, A. Fleisher, H. Fleurbaey, A. Foltynowicz, T. Furtenbacher, J. Harrison, J. Hartmann, V. Horneman, X. Huang, T. Karman, J. Karns, S. Kassi, I. Kleiner, V. Kofman, F. Kwabia-Tchana, N. Lavrentieva, T. Lee, D. Long, A. Lukashevskaya, O. Lyulin, V. Makhnev, W. Matt, S. Massie, M. Melosso, S. Mikhailenko, D. Mondelain, H. Müller, O. Naumenko, A. Perrin, O. Polyansky, E. Raddaoui, P. Raston, Z. Reed, M. Rey, C. Richard, R. Tóbiás, I. Sadiek, D. Schwenke, E. Starikova, K. Sung, F.

Tamassia, S. Tashkun, J. Vander Auwera, I. Vasilenko, A. Vigasin, G. Villanueva, B. Vispoel, G. Wagner, A. Yachmenev, and S. Yurchenko, J. Quant. Spectrosc. Radiat. Transfer **277**, 107949 (2022).

[41] T. Delahaye, R. Armante, N. Scott, N. Jacquinet-Husson, A. Chédin, L. Crépeau, C. Crevoisier, V. Douet, A. Perrin, A. Barbe, V. Boudon, A. Campargue, L. Coudert, V. Ebert, J.-M. Flaud, R. Gamache, D. Jacquemart, A. Jolly, F. Kwabia Tchana, A. Kyuberis, G. Li, O. Lyulin, L. Manceron, S. Mikhailenko, N. Moazzen-Ahmadi, H. Müller, O. Naumenko, A. Nikitin, V. Perevalov, C. Richard, E. Starikova, S. Tashkun, V. Tyuterev, J. Vander Auwera, B. Vispoel, A. Yachmenev, and S. Yurchenko, J. Mol. Spectrosc. **380**, 111510 (2021).

[42] F. Thibault, K. Patkowski, P. S. Żuchowski, H. Jóźwiak, R. Ciuryło, and P. Wcisło, J. Quant. Spectrosc. Radiat. Transfer **202**, 308 (2017).

[43] H. Jóźwiak, F. Thibault, N. Stolarczyk, and P. Wcisło, J. Quant. Spectrosc. Radiat. Transfer **219**, 313 (2018).

[44] R. Z. Martínez, D. Bermejo, F. Thibault, and P. Wcisło, J. Raman Spectrosc. **49**, 1339 (2018).

[45] F. Thibault, R. Z. Martínez, D. Bermejo, and P. Wcisło, Mole. Astrophys. **19**, 100063 (2020).

[46] G. Kowzan, P. Wcisło, M. Słowiński, P. Masłowski, A. Viel, and F. Thibault, J. Quant. Spectrosc. Radiat. Transfer **243**, 106803 (2020).

[47] G. Kowzan, H. Cybulski, P. Wcisło, M. Słowiński, A. Viel, P. Masłowski, and F. Thibault, Phys. Rev. A **102**, 012821 (2020).

[48] M. Słowiński, F. Thibault, Y. Tan, J. Wang, A.-W. Liu, S.-M. Hu, S. Kassi, A. Campargue, M. Konefał, H. Jóźwiak, K. Patkowski, P. Żuchowski, R. Ciuryło, D. Lisak, and P. Wcisło, Phys. Rev. A **101**, 052705 (2020).

[49] K. Stankiewicz, H. Jóźwiak, M. Gancewski, N. Stolarczyk, F. Thibault, and P. Wcisło, J. Quant. Spectrosc. Radiat. Transfer **254**, 107194 (2020).

[50] E. Serov, N. Stolarczyk, D. Makarov, I. Vilkov, G. Y. Golubiatnikov, A. Balashov, M. Koshelev, P. Wcisło, F. Thibault, and M. Y. Tretyakov, J. Quant. Spectrosc. Radiat. Transfer **272**, 107807 (2021).

[51] M. Słowiński, H. Jóźwiak, M. Gancewski, K. Stankiewicz, N. Stolarczyk, Y. Tan, J. Wang, A.-W. Liu, S.-M. Hu, S. Kassi, A. Campargue, K. Patkowski, P. Żuchowski, R. Ciuryło, F. Thibault, and P. Wcisło, J. Quant. Spectrosc. Radiat. Transfer **277**, 107951 (2022).

[52] N. Stolarczyk, G. Kowzan, F. Thibault, H. Cybulski, M. Słowiński, Y. Tan, J. Wang, A.-W. Liu, S.-M. Hu, and P. Wcisło, J. Chem. Phys. **158**, 094303 (2023).

[53] P. Wcisło, F. Thibault, M. Zaborowski, S. Wójtewicz, A. Cygan, G. Kowzan, P. Masłowski, J. Komasa, M. Puchalski, K. Pachucki, R. Ciuryło, and D. Lisak, J. Quant. Spectrosc. Radiat. Transfer **213**, 41 (2018).

[54] M. Lamperti, L. Rutkowski, D. Ronchetti, D. Gatti, R. Gotti, G. Cerullo, F. Thibault, H. Jóźwiak, S. Wójtewicz, P. Masłowski, P. Wcisło, D. Polli, and M. Marangoni, Commun. Phys. **6**, 67 (2023).

[55] D. Paredes-Roibás, R. Z. Martínez, H. Jóźwiak, and F. Thibault, J. Quant. Spectrosc. Radiat. Transfer **275**, 107868 (2021).

[56] G. Knizia, T. B. Adler, and H.-J. Werner, J. Chem. Phys. **130**, 054104 (2009).

[57] K. A. Peterson, T. B. Adler, and H.-J. Werner, J. Chem. Phys. **128**, 084102 (2008).

[58] D. Feller, K. A. Peterson, and T. D. Crawford, J. Chem. Phys. **124**, 054107 (2006).

[59] H.-J. Werner, P. J. Knowles, G. Knizia, F. R. Manby, and M. Schütz, Wiley Interdiscip. Rev.: Comput. Mol. Sci. **2**, 242 (2012).

[60] F. Dumouchel, E. Quintas-Sánchez, C. Balança, R. Dawes, F. Lique, and N. Feautrier, J. Chem. Phys. **158**, 164307 (2023).

[61] A. Zadrożny, H. Jóźwiak, E. Q.-S. Ernesto, R. Dawes, and P. Wcisło, J. Chem. Phys. **157**, 174310 (2022).

[62] O. Denis-Alpizar, E. Quintas-Sánchez, and R. Dawes, Mon. Not. R. Astron. Soc. **512**, 5546 (2022).

[63] Y. Ajili, E. Quintas-Sánchez, B. Mehnen, P. S. Żuchowski, F. Brzęk, N. El-Kork, M. Gacesa, R. Dawes, and M. Hochlaf, Phys. Chem. Chem. Phys. **24**, 28984 (2022).

[64] E. Quintas-Sánchez and R. Dawes, J. Chem. Inf. Model. **59**, 262 (2019).

[65] R. Dawes and E. Quintas-Sánchez, *Reviews in Computational Chemistry* (John Wiley & Sons, Inc., 2018), Vol. 31, Chap. 5, pp. 199–264.

[66] M. Majumder, S. A. Ndengué, and R. Dawes, Mol. Phys. **114**, 1 (2016).

[67] R. Dawes, X.-G. Wang, A. W. Jasper, and T. Carrington, Jr., J. Chem. Phys. **133**, 134304 (2010).

[68] I. M. Sobol, USSR Comput. Math. Math. Phys. **16**, 236 (1976).

[69] R. Dawes, X. G. Wang, and T. Carrington, J. Phys. Chem. A **117**, 7612 (2013).

[70] H. Jóźwiak, F. Thibault, H. Cybulski, and P. Wcisło, J. Chem. Phys. **154**, 054314 (2021).

[71] S. Green, J. Chem. Phys. **62**, 2271 (1975).

[72] M. Gancewski, H. Jóźwiak, E. Quintas-Sánchez, R. Dawes, F. Thibault, and P. Wcisło, J. Chem. Phys. **155**, 124307 (2021).

[73] J. M. Launay, J. Phys. B: At. Mol. Phys. **10**, 3665 (1977).

[74] M. H. Alexander and A. E. DePristo, J. Chem. Phys. **66**, 2166 (1977).

[75] J. V. Lill, G. A. Parker, and J. C. Light, Chem. Phys. Lett. **89**, 483 (1982).

[76] J. A. Coxon and P. G. Hajigeorgiou, J. Quant. Spectrosc. Radiat. Transfer **151**, 133 (2015).

[77] G. Cazzoli and C. Puzzarini, J. Mol. Spectrosc. **226**, 161 (2004).

[78] P. G. Hajigeorgiou, J. Chem. Phys. **138**, 014309 (2013).

[79] H. Rabitz, J. Chem. Phys. **63**, 5208 (1975).

[80] B. R. Johnson, J. Chem. Phys. **69**, 4678 (1978).

[81] H. Jóźwiak, M. Gancewski, A. Grabowski, K. Stankiewicz, A. Zadrożny, A. Olejnik, and P. Wcisło, BIGOS Computer Code.

[82] L. Monchick and L. Hunter, J. Chem. Phys. **85**, 713 (1986).

[83] J. Schaefer and L. Monchick, Astron. Astrophys. **265**, 859–868 (1992); available at https://ui.adsabs.harvard.edu/abs/1992A%26A...265..859S/abstract.

[84] A. P. Yutsis, I. B. Levinson, and V. V. Vangas, *Theory of Angular Momentum* (Israel Program for Scientific Translations, Jerusalem, 1962).

[85] A. Ben-Reuven, Phys. Rev. **141**, 34 (1966).

[86] A. Ben-Reuven, Phys. Rev. **145**, 7 (1966).

[87] G. C. Corey and F. R. McCourt, J. Chem. Phys. **81**, 2318 (1984).

[88] P. Wcisło, F. Thibault, H. Cybulski, R. Ciuryło, A. Cygan, G. Kowzan, P. Masłowski, J. Komasa, M. Puchalski, K. Pachucki, R. Ciuryło, and D. Lisak, Phys. Rev. A **91**, 052505 (2015).

[89] L. Gomez, S. V. Ivanov, O. G. Buzykin, and F. Thibault, J. Quant. Spectrosc. Radiat. Transfer **112**, 1942–1949 (2011).

[90] F. Thibault, R. Z. Martínez, D. Bermejo, and L. Gómez, J. Quant. Spectrosc. Radiat. Transfer **112**, 2542 (2011).

[91] N. Stolarczyk, F. Thibault, H. Cybulski, H. Jóźwiak, G. Kowzan, B. Vispoel, I. Gordon, L. Rothman, R. Gamache, and P. Wcisło, J. Quant. Spectrosc. Radiat. Transfer **240**, 106676 (2020).

[92] P. Wcisło, F. Thibault, N. Stolarczyk, H. Jóźwiak, M. Słowiński, M. Gancewski, K. Stankiewicz, M. Konefał, S. Kassi, A. Campargue, Y. Tan, J. Wang, K. Patkowski, R. Ciuryło, D. Lisak, R. Kochanov, L. Rothman, and I. Gordon, J. Quant. Spectrosc. Radiat. Transfer **260**, 107477 (2021).

[93] K. Stankiewicz, N. Stolarczyk, H. Jóźwiak, F. Thibault, and P. Wcisło, J. Quant. Spectrosc. Radiat. Transfer **276**, 107911 (2021).

[94] F. Rohart, H. Mäder, and H. Nicolaisen, J. Chem. Phys. **101**, 6475 (1994).

[95] H. M. Pickett, J. Chem. Phys. **73**, 6090 (1980).

[96] P. Wcisło, I. E. Gordon, H. Tran, Y. Tan, S. M. Hu, A. Campargue, S. Kassi, D. Romanini, C. Hill, R. V. Kochanov, and L. Rothman, J. Quant. Spectrosc. Radiat. Transfer **177**, 75 (2016).

[97] J. O. Hirschfelder, C. F. Curtiss, and R. B. Bird, *The Molecular Theory of Gases and Liquids* (Wiley, 1954).

[98] S. Chapman and T. G. Cowling, *The Mathematical Theory of Non-Uniform Gases* (Cambridge University Press, 1939).